RSC Advances

PAPER

Cite this: *RSC Adv.*, 2015, **5**, 30260

Three dimensional carbon nanotube/nickel hydroxide gels for advanced supercapacitors†

Hanlin Cheng and Hai M. Duong*

Received 30th January 2015
Accepted 23rd March 2015

DOI: 10.1039/c5ra01847a

www.rsc.org/advances

In this work, we have successfully developed three-dimensional (3D) nickel hydroxide ($Ni(OH)_2$)/single-walled carbon nanotube (SWNT) gel composites for supercapacitor applications. The composites are prepared using a facile coating-aging method followed by an electrochemical deposition. The obtained SWNT gels and their derived $Ni(OH)_2$/SWNT composites present 3D network structures composed of randomly orientated nanotube bundles. It is found that the sizes of these bundles can be easily tuned using two different drying techniques. The directly dried $Ni(OH)_2$/SWNT composites with seriously bundled nanotubes are capable of maintaining an excellent discharge performance as well as a satisfactory cycling stability. The improved electrochemical performance of the $Ni(OH)_2$/SWNT xerogel composite comes from a 3D SWNT conductive highway and a stronger $Ni(OH)_2$/SWNT interface bonding. In contrast, the hydrogel composite prepared in the absence of a drying process, despite achieving both high areal and mass-based capacitance, suffers a severe cycling drop. Compared with 3D graphene and its derived composites, our composite design with the employment of 1D SWNTs has the merit of shorter ion diffusion distances which offers a distinctive opportunity for the future development of 3D electrodes.

1 Introduction

To overcome the challenges from the energy crisis and environmental contamination, both advanced energy generators and environmentally-benign energy storage techniques are needed. Compared with the industrial-scale storage systems utilizing compressed air or pumped hydro-power, electrochemical energy storage (EES) devices such as fuel cells, batteries and supercapacitors (SCs) can be developed for portable electronic devices, rendering them the ideal power sources for next generation vehicles.[1]

Among different types of the EES devices, SCs have attracted great attention recently due to their moderate energy and high power densities.[2] Generally, SCs can be classified into two types based on their working mechanisms. The first type of the SCs is the electrochemical double layer capacitor (EDLC) which stores energy through physical ions adsorption at the interface between the electrode and electrolyte. The EDLCs can possess a long term cycling stability up to 10 000 cycles.[3] However, the energy density of the EDLCs is much lower than that of lithium ion batteries which greatly limit their marketing proceedings.[4] The second type of the SCs is the pseudocapacitor which involves redox couples to increase its energy density. Due to the redox nature of the pseudocapacitors, volume changes caused by phase transformation during working processes inevitably damages electrode cycling lives.[5] In order to combine the merits of two SC types and to increase the energy density by extending the potential window, hybrid SCs have been recently developed by employing an EDLC electrode against a pseudocapacitance one.[6] Although most of the hybrid SCs has applied aqueous electrolytes to deliver high conductivities, hybrid SCs works in organic electrolytes were also investigated.[7–9]

Besides the configuration, the key element for enhancing device performance is to improve the electron and ion transport during charge/discharge process.[10] To achieve this goal, various binderless 3D electrodes were developed.[11–14] It is supposed that electrical conductivities of the 3D structures would be greatly increased in the absence of insulating polymer binders. Simultaneously, pores established inside the 3D structures would serve as electrolyte reservoirs to facilitate the ion transport. Gong *et al.*[15] have developed a carbon nanotube/$Ni(OH)_2$ core–shell structure on a nickel foam, which was used as a positive electrode for the hybrid SCs. Similarly, metal oxides possessing high electrical conductivities such as cobalt oxide were also designed into the core–shell structure for the electrode applications.[16] Recently, 3D layered composite electrodes using graphene coated nickel foam have been synthesized through either electrophoretic[17,18] or chemical vapour deposition.[19,20] The graphene coated electrodes can enhance the interface bonding of the host/guest materials to improve their electrochemical stabilities. In order to reduce the total weight of

Department of Mechanical Engineering, National University of Singapore, 9 Engineering Drive 1, EA-07-05, 117575 Singapore. E-mail: mpedhm@nus.edu.sg; Fax: +6565161567; Tel: +6567791459

† Electronic supplementary information (ESI) available: FESEM, TEM and electrochemical performances. See DOI: 10.1039/c5ra01847a

the electrodes, nickel foam can also be etched away to obtain a 3D graphene network.[19,20] In spite of the nickel foams, carbon foams derived from polymer carbonization were recently used directly as the scaffolds for the 3D electrodes.[21–23]

Nevertheless, methods mentioned above merely resulted in a thin layer of materials on the 3D backbone surface where leaving most macropores inside nickel foam unused, which usually leads to small areal and volumetric capacitance. For example, although Yang *et al.* has achieved an ultrahigh specific capacitance of 3125 F g^{-1}, the areal capacitance is merely 1.6 F cm^{-2} due to a small mass loading.[12] Also, consider the fact the ion transport and capacitance behaviour are greatly influenced by pores in ranges of meso-scale or nano-scale,[24] it is necessary to give intense efforts to better tune the pore size distributions. Based on that, 3D mesoporous network such as graphene hydrogel/xerogels[25] and carbon aerogels[26] were developed for the supercapacitor applications. Xu *et al.*[27] synthesized a graphene hydrogel thin film for the SC application with a capacitance of 186 F g^{-1} and found that the capacitance unfortunately decreased with the increase of the film thickness for elongated electron and ion transport pathways. To further improve the electron and ion transport, graphene gels were successfully incorporated inside the nickel foam and were used as the SC electrode.[28–30] With the similar concept to reduce the electrode weight, the nickel foams were then etched to obtain the pure graphene gel.[30,31] Unfortunately, the free-standing graphene gels suffered a low electrical conductivity and poor mechanical strength. For a stronger but lighter electrode development, partial etch of the nickel foam was applied.[32] Besides the single component materials, graphene derived aerogel/hydrogel composites were also used for the SC electrodes, achieving capacitances over 1000 F g^{-1}.[33–38]

Compared with the gel made of 2D graphene layers, it is believed that gels made of 1D SWNTs can significantly increase the electrochemical performance of the SCs due to the excellent multifunctional properties[39–43] and the quicker ion diffusion.[44] However, the SWNT-gel structures have seldom reported in the usage for the SC electrode development.[45] Here we report a successful fabrication of a novel structure of pristine SWNT gels and their derived $Ni(OH)_2$/SWNT gel composites for the supercapacitor applications. The prepared xerogel composite is able to achieve a both high specific capacitance (1289 F g^{-1}) and areal capacitance (3.1 F cm^{-2}).

2 Experimental

2.1 Materials

SWNTs consisting of one third of metallic SWNTs, two thirds of semiconducting SWNTs and 5–30 μm in length, were purchased from Chengdu Organic Chemicals Co Ltd. Nickel nitrate hexahydrate and sodium dodecylbenzene sulfonate (SDBS) were purchased from the Sigma Aldrich. Hydrochloric acid (HCl ~37%) and absolute ethanol were purchased from the Merck Pte Ltd. Nickel foams with thickness of 1.2 mm were bought from the MTI Corporation.

Before synthesizing the gels and composites, SWNTs were purified by soaking them in HCl (1 M) at 60 °C for 12 h to remove the remaining iron catalyst. Then the treated SWNTs were washed with large amount of DI water and filtrated before drying. The nickel foams were washed by using ethanol and DI water in sequence before the usage.

2.2 Synthesis of SWNT gels and $Ni(OH)_2$/SWNT gel composites

The SWNT xerogels and hydrogels synthesized through a facile coating-aging method. The mixture consisting of 25 mg SWNT and 125 mg SDBS was firstly dispersed in 5 mL DI water by a probe sonication. Next, the nickel foam was immersed into the SWNT suspension and underwent bath sonication for 10 min to fill all pores of the nickel foams with SWNTs. After one-day aging, the prepared hydrogel was subsequently washed by the DI water continuously for one week to remove all surfactants. To obtain the SWNT xerogel, prepared SWNT hydrogel samples were then dried in a fumehood for another week.

To prepare the $Ni(OH)_2$/SWNT xerogel composite, the SWNT xerogel was initially rinsed with ethanol and DI water in sequence for a wetting purpose. Afterwards, $Ni(OH)_2$ was grown on the SWNT xerogel by a simple electrodeposition method.[12] In brief, the SWNT xerogel was deposited under −0.7 V (*vs.* Ag/AgCl) in a 0.1 M $Ni(NO_3)_2$ plating solution until total charges reached desired amount. The achieved $Ni(OH)_2$/SWNT xerogel composite was washed by DI water and dried at 60 °C for 12 h. The obtained SWNT xerogel composite was named as NiC-xero-*X*, where *X* denotes the charges passed during the $Ni(OH)_2$ deposition.

The $Ni(OH)_2$/SWNT hydrogel composite, named as NiC-hydro, was prepared similarly using the above method in the absence of drying step. The water inside the SWNT hydrogel was exchanged with the plating solution before the $Ni(OH)_2$ deposition. For comparison, $Ni(OH)_2$ was also directly deposited on the nickel foam using the same protocol. Without further indication, the total electrical charges passed for the $Ni(OH)_2$ deposition were 3.33 C. The mass loading of the SWNT and $Ni(OH)_2$ is obtained based on the comparison between the total mass of the materials and nickel foam with an analytical balance in accuracy of 0.01 mg. The mass loading of the SWNT gels was 0.5–1 mg cm^{-2} and that of the whole composites was about 2–2.5 mg cm^{-2}.

2.3 Characterization

Crystal structures of the as-prepared SWNT gels/composites were identified by powder X-ray diffraction (XRD) on Shimazu X-ray diffractometer 6000 with Cu Kα radiation ($k = 1.5418$ Å) between 10° and 80° at a scan rate of 1.2° min^{-1}. The morphologies of the SWNT gels and $Ni(OH)_2$/SWNT gel composites were investigated by a field emission scanning electron microscopy (FESEM Hitachi S4300). Prior to FESEM imaging, the SWNT hydrogels were dried using supercritical carbon dioxide. Transmission electron microscopy (TEM) together with selected area electron diffraction (SAED) was performed on JEOL 3010 transmission electron microscope to further investigate the composite microstructures.

2.4 Electrochemical measurements

The composite deposited nickel foams were directly used as the SC electrodes without the addition of any polymer binders or carbon additives. A platinum plate (1 cm^2) was used as the counter electrode and the saturated calomel electrode (SCE) was selected as a reference electrode. All tests were conducted in a 1 M KOH solution with a three-electrode configuration. Cyclic voltammetry (CV) and Galvanostatic charge/discharge (GCD) were tested using Solartron 1287 electrochemical workstation equipped with a Solartron 1260 frequency response analyzer. The electrochemical impedance spectroscopy (EIS) was applied to characterize kinetic properties of the samples in the frequency ranges of 0.01–100 000 Hz at an amplitude of 5 mV against the open circuit voltage. The cycling performance was tested using the battery test system from Neware Technology Ltd. The specific capacitance was calculated based on the following equations.

From CV,

$$C_s = \frac{\int I\,dV}{2mv\Delta V} \quad (1)$$

From GCD,

$$C_s = \frac{I\Delta t}{m\Delta V} \quad (2)$$

where: I is the current, v is the scan rate, V is the potential window, Δt is the discharge time and m is the total mass of tested materials including both SWNTs and $Ni(OH)_2$. For the calculation of the areal specific capacitance, m is replaced with the apparent electrode area. Integration is calculated from 0–0.6 V based on the whole CV loop.

3 Results and discussion

3.1 Mechanisms of the 3D structure formation of the SWNT gels and composites

The network structures of the SWNT hydrogels can be easily achieved by a coating-aging method as schemed in Fig. 1. During the gelation, the individual SWNTs form a 3D randomly-oriented SWNT network due to van der Waals force[39] and osmotic pressure of SDBS-formed micelles.[46] In this stage, the van der Waals force mainly plays two roles. It not only helps to cause the percolation of nanotubes to form a 3D structure but also inevitably bring the bundling of the individual nanotubes.

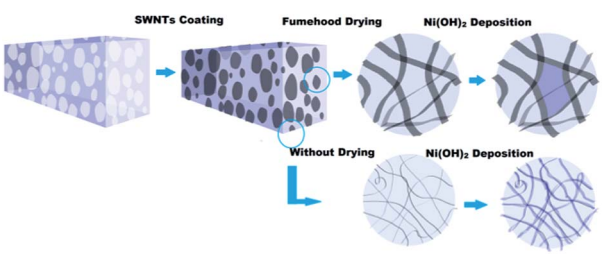

Fig. 1 Schemed synthesis procedures of the $Ni(OH)_2$/SWNT xerogel and $Ni(OH)_2$/SWNT hydrogel composite.

For hydrogels obtained without the drying process, SWNTs are much less bundled and could preserve their original structures. While for the SWNT xerogels prepared after drying in fume-hood, the individual SWNTs tends to seriously bundle together due to the capillary force because of the evaporation of water inside. When fabricating the composites by depositing $Ni(OH)_2$ in either hydrogel or xerogels, nitrite ions are firstly reduced under negative potential to generate hydroxyl ions and raise the local pH. Simultaneously, precipitation of $Ni(OH)_2$ occurs inside the gels according to following chemical equations.[47]

$$NO_3^- + 7H_2O + 8e^- \rightarrow NH_4^+ + 10OH^- \quad (3)$$

$$Ni^{2+} + 2OH^- \rightarrow Ni(OH)_2\downarrow \quad (4)$$

3.2 Structural properties and composition

Fig. 2a depicts the purchased nickel foam with an average large pore size of ~150 μm. Fig. 2b exhibits the SWNT xerogel consisting of the randomly oriented nanotube bundles with width varying from 20 to 80 nm. A porous structure presented in xerogels is ideal for the ion transport. The morphology of the SWNT hydrogel is shown in the Fig. 2c. Different from the xerogels, the hydrogel is composed of either individual nanotube or slighter bundled nanotubes which are reported previously.[39,42,43] Compared with the xerogels, such kind of structure has a higher surface area, but the inhomogeneity of the nanotubes distribution may hazard the electrode performance. The structures of the deposited $Ni(OH)_2$, NiC-xero and NiC-hydro are

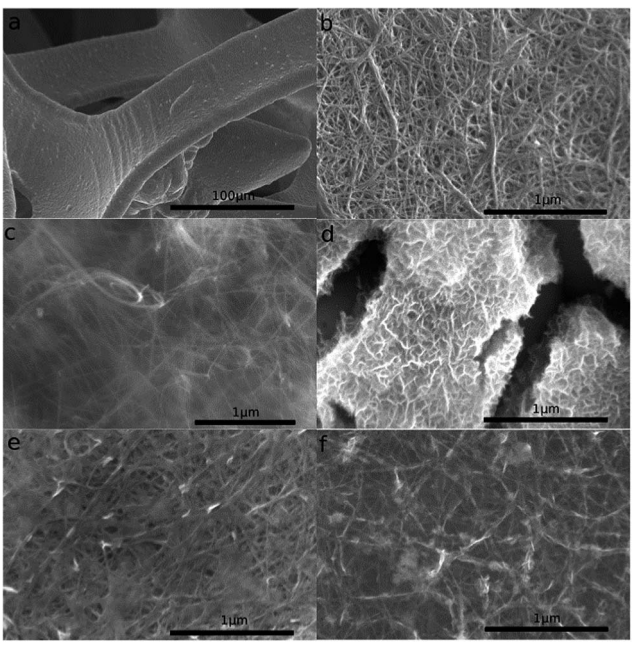

Fig. 2 FESEM images of (a) the nickel foam (b) SWNT xerogel (c) SWNT hydrogel (d) $Ni(OH)_2$ deposited at nickel foam (e) $Ni(OH)_2$/SWNT xerogel (NiC-xero) composite and (f) $Ni(OH)_2$/SWNT hydrogel (NiC-hydro) composite.

shown in Fig. 2d–f. When deposited directly on the nickel foam, $Ni(OH)_2$ present severe aggregates consisting of self-assembled nanoflakes (Fig. 2d). While the SWNT xerogel composite in Fig. 2e display a porous structure with the embedded $Ni(OH)_2$ flakes. SWNT bundles not only preserve the original structure in xerogels but also play an important role in preventing the aggregation of the active materials. What is more, the less stiff nanotube bundles would serve a buffer layer to accommodate the volume changes of nickel hydroxide, which help to maintain the rigidity of the electrode. For NiC-hydro shown in Fig. 2f, $Ni(OH)_2$ flakes grow along SWNTs to form the core–shell structure. The inhomogeneously decorated hydroxides inherit the pre-prepared hydrogel structure. We purpose the apparent morphology difference between NiC-xero and NiC-hydro can be explained by the following reason. During the deposition of nickel hydroxide, the small surface curvature and large pores of the SWNT xerogel are able to facilitate the ion transport during the $Ni(OH)_2$ growth. As a result, the $Ni(OH)_2$ is embedded into the SWNT pores. In contrast, smaller pores together with narrow sized SWNT bundles in hydrogel gives a large curvature, causing a quick depletion of the nickel ions near bundle surface, leads to the hetero-nucleation of the $Ni(OH)_2$ to form the core–shell structure along nanotube bundles.

Compared with the pure $Ni(OH)_2$ directly deposited at the nickel foam, our electrode design has the merit of the high utilization of the pores inside the nickel foam. In Fig. S1a,† $Ni(OH)_2$ only stays at the nickel foam backbone to form a quasi 3D structure. Nevertheless, SWNTs in the hydrogel and xerogel composites can fill completely the macropores of the nickel foam to establish an inner micro-conductive network (Fig. S1b–e†). Unlike other carbon-based xerogels, the developed SWNT xerogels in this work are able to preserve their 3D structures with minor collapse. The improved structural stability is attributable to a synergistic effect between the macro-network of the nickel foam and the micro-network of SWNTs. To confirm that the prepared gels have achieved 3D structure, we have cut the samples using sharp knife carefully and observe their sectional area. Images shown in Fig. S2† clearly demonstrate that the 3D nanotube network structure locates both at the surface and inside the nickel foam.

To control the morphology of the NiC-xero composites, we have varying the deposition charges during the material synthesis and the corresponding results are presented in Fig. S3a–d.† $Ni(OH)_2$ partially fills the pores under the small deposition charge (Fig. S3a†) and generate various mesopores in the xerogels. When the deposition charge further increases to 3.33 C, the pores are almost fully occupied by $Ni(OH)_2$ (Fig. S3b†) and some hydroxides even start to grow out of xerogel seen in the white flake in the bottom left corner of the image. Without surprise, we find a further increase of $Ni(OH)_2$ concentration also causes serious aggregates (Fig. S3c†), resembling the pure $Ni(OH)_2$ deposited on the nickel foam. This phenomenon could explained by that with internal stress created during the $Ni(OH)_2$ growth, xerogel would be separated to several thin layers. Then, the $Ni(OH)_2$ would overflow from the each thin xerogel layer and agglomerate between them. Finally, as shown in Fig. S3d,† when deposition charge increases to 7.77 C, thicker $Ni(OH)_2$ flakes can be observed more clearly. The structure evolution presented above indicates the limiting capability of SWNTs in preventing $Ni(OH)_2$ aggregation.

Fig. 3 shows the typical TEM images of the NiC-xero and NiC-hydro composite. For the xerogel composites (Fig. 3a), ultrathin nickel hydroxide flakes are successfully incorporated into the nanotube scaffold which is in consistent with the previous SEM images. From a more detailed observation, we see that the $Ni(OH)_2$ actually would not completely block the pores in the SWNT scaffold. The small intervals reserved between the hydroxides and SWNT bundles play an important role in the ion diffusion. While in NiC-hydro composite (Fig. 3b), nano-flaky $Ni(OH)_2$ with minor aggregations grow along the SWNTs bundles to form an inhomogeneous structure. This kind of architecture may also achieve and good electron transport but, unlike the NiC-xero composite, might has poor long term stability since SWNTs merely connect nickel hydroxide in one edge. From higher magnification images shown in Fig. S4a and b,† nanotube bundles in xerogels consist of has 40–80 individual SWNTs while in hydrogels, typically 5–10 individual SWNTs help to compose the nanotube bundles. Consider the same statistic distributions of both metallic and semiconducting nanotubes, the larger bundles in xerogels are supposed to deliver higher conductance simply for containing more metallic bundles. The diffraction rings in the SAED images of the NiC-hydro (Fig. S4c†) and NiC-xero (Fig. S4d†) show the existence of both α and β-$Ni(OH)_2$. For the NiC-xero composites, the (003), (006), (009), (101) crystal planes from α-$Ni(OH)_2$ and (102), (201) planes from β-$Ni(OH)_2$ are found. For the hydrogel composites, the diffractions can be assigned to the (003), (014), (110) planes of α-$Ni(OH)_2$ and (201) plane of the β-$Ni(OH)_2$.

The crystal structures of the prepared samples have also been investigated by employing XRD (Fig. 4). The peaks of the NiC-xero located at 11.2° and 34.0° can be assigned to the (003) and (012) planes of α-$Ni(OH)_2$. The broad peaks from 20° to 30° are related to the SWNT bundles.[48] In NiC-hydro composite peaks corresponding to the (003) and (006) crystal planes of α-$Ni(OH)_2$ can be found located at 14.4° and 28.5°. The left shifted (003) peaks reflect a larger lattice distance of the correspondent crystal plane based on the Bragg's equation, indicating a less packed crystal structure. This kind of structural changes might

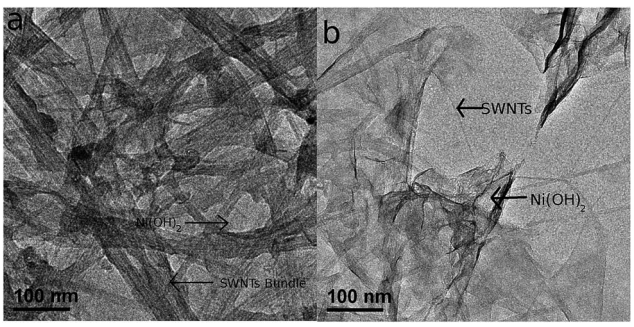

Fig. 3 TEM images of (a) the $Ni(OH)_2$/SWNT xerogel (NiC-xero) composite and (b) $Ni(OH)_2$/SWNT hydrogel (NiC-hydro) composite.

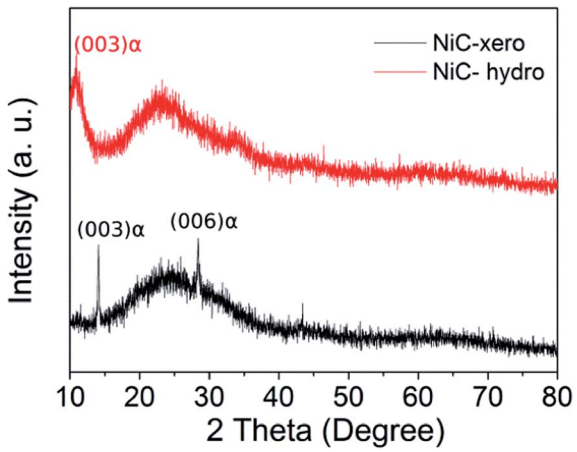

Fig. 4 XRD pattern of the $Ni(OH)_2$/SWNT xerogel composite (black line) and the $Ni(OH)_2$/SWNT hydrogel composite (red line).

arise from a harsh growth environment in the hydrogels where nucleation has been limited due to the over narrowed SWNT bundles. Also, it is worth noting that peaks in hydrogel are much more broadening than those in xerogels, indicating smaller grain sizes. Different from the SAED images, β-$Ni(OH)_2$ is not detected in XRD which is probably due to its small percentage and inhomogeneous distribution.

3.3 Electrochemical evaluation

The electrochemical performance of the SWNT-xerogel and -hydrogel are displayed in Fig. 5a and b. The nearly rectangular shape of the CV curves clearly indicates a double layer capacitance coming from the ion adsorption at the interface between SWNTs and the electrolyte. CV shapes maintain a good shape even when increasing the scan rate to 500 mV s^{-1}, reflecting an excellent electrical conductivity of the SWNT network of both hydrogel and xerogel. The calculated specific capacitances are shown in the Fig. 5c. For xerogels, it can reach 36 F g^{-1} at 2 mV s^{-1} while for hydrogel, merely 23 F g^{-1} could be achieved

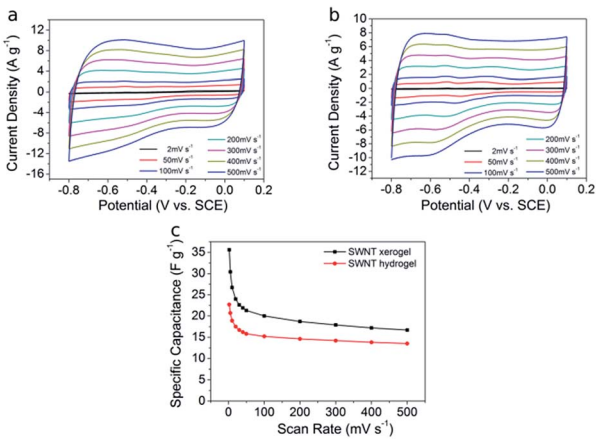

Fig. 5 CV results tested at different scan rate (a) SWNT xerogel (b) SWNT hydrogel and (c) corresponding specific capacitance.

at the same scan rate. A better electrochemical performance in xerogels can be attributed to a much more homogeneous structure and higher electrical conductance of SWNT bundles.

Fig. 6 shows the electrochemical performance of the $Ni(OH)_2$ and $Ni(OH)_2$/SWNT gel composites. Seen from the CV curves in Fig. 6a, both pristine $Ni(OH)_2$ and $Ni(OH)_2$ gel composite exhibit redox peak pairs which can be explained by the following equation[49]

$$Ni(OH)_2 + OH^- \leftrightarrow NiOOH + H_2O + e^- \quad (5)$$

compared with the pure hydroxides and pure SWNT gels (Fig. S4†), both NiC-xero and NiC-hydro composites present higher specific capacitance for a larger enclosed area. A smaller polarization in the NiC-xero compared with NiC-hydro and $Ni(OH)_2$ can be ascribed to a better composite conductivity. Fig. 6b presents the specific capacitance calculated from the CV curve. The directly deposited $Ni(OH)_2$, the NiC-xero and the NiC-hydro deliver specific capacitances of 899, 1221, 1124 F g^{-1} at 2 mV s^{-1}, respectively. Although achieving a high specific capacitance at a low scan rates, the $Ni(OH)_2$ gel composites encounter a drop of specific capacitance at higher scan rates due to the limited ion and electron transport.[50] Fig. 6c gives the charge/discharge profiles of the prepared samples. The observed flat plateaus similarly demonstrate a redox charge/discharge process. Compared with the direct deposited $Ni(OH)_2$, the delicately engineered $Ni(OH)_2$/SWNT gel composite gives a better performance of longer discharge time, suggesting a higher specific capacitance. The specific capacitances of the $Ni(OH)_2$, the NiC-xero and NiC-hydro composites are 785, 1289 and 1409 F g^{-1} at 4 mA cm^{-2} (Fig. 6d). Among three kinds of structures, NiC-xero has achieved the optimized electrochemical performance for both a satisfied low rate capacitance and good high rate retention. Although the NiC-hydro composite presents the highest specific capacitance at low discharge rates, it deteriorates quickly at the larger

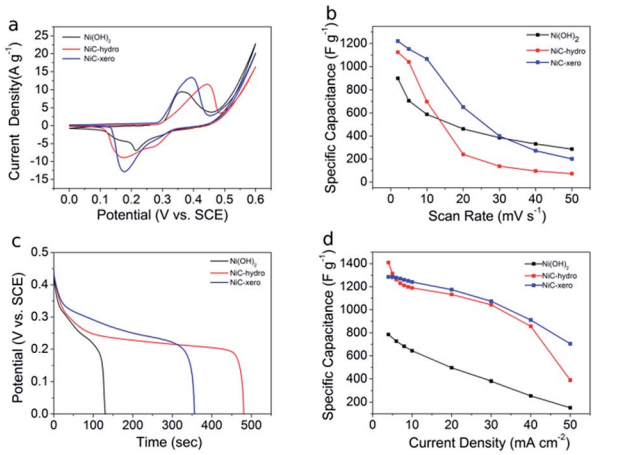

Fig. 6 Electrochemical performance of various gel composites: (a) CV curves of various gel composites (b) specific capacitance calculated from different scan rates (c) discharge profiles of $Ni(OH)_2$, NiC-xero and NiC-hydro composites and (d) specific capacitances obtained from different galvanic discharge rates.

discharge rates. The improvement of NiC-xero composite can be attributed to better electrical conductivities and homogeneous distribution of the larger SWNT bundles. It is also worth noting that the CV and GCD test present a discrepancy of the specific capacitance changes. The electrochemical performance is determined by the electron and ion transport. The SWNT network helps to facilitate the electron transport and improve the electrical conductivity of the electrode. However, nanopores formed by the randomly-orientated may hinder the ion transport and render the $Ni(OH)_2$ surpass the NiC-xero over 30 mV s^{-1}. Considering most electronic devices work at a near constant current, the GCD may reflect the performance better than CV in practical applications as seen in Fig. 6d. Thus, the xerogel composite has a better capacitance performance.

The effects of the $Ni(OH)_2$ loading in the SWNT-xerogel composite on the electrochemical performance are presented in Fig. S5.† The increase of the $Ni(OH)_2$ decreases the electrode conductivity and brings a larger polarization as seen in the CV curves (Fig. S5a†). The specific capacitances from the different scan rates are summarized in Fig. S5b.† The NiC-xero-1.11 C composite gives the most excellent capacitance retention at high discharge rates but suffers from a low specific capacitance due to a small $Ni(OH)_2$ loading in composite. Fig. S5c and d† present the charge/discharge performance and corresponding specific capacitances. The NiC-xero-3.33 composite has the optimized results of both the satisfying capacitance and the high rate capacitance retention. Increasing hydroxides deposition charges leads to the hydroxide aggregation which renders electrode suffer a fast capacitance loss at the higher discharge rate. The decreased specific capacitance can be also explained by the previous SEM images. Although Fig. S3d† exhibits a nanoflaky structure and high areal capacitance (F cm^{-2}), but it suffers from a quick drop. The quick drop of capacitance at high discharge rate is because of longer electron pathways. For the NiC-xero-3.3, electron only needs to reach embedded $Ni(OH)_2$ from the conductive SWNTs network. However, for the NiC-xero-7.7, elections have to transport from the SWNT to the embedded $Ni(OH)_2$ and then to the nano-flaky $Ni(OH)_2$ seen in the SEM images, which leads to low material utilization.

To prove the success of our novel composite structure, we also present the areal capacitances of work in Fig. S6.† Values achieved here much higher than previous works[35–38] of MnO_2/graphene aerogel composites and the $Ni(OH)_2$ counterpart[12,51] as well as competitive to $Ni(OH)_2$/graphene aerogel composites.[34] For $Ni(OH)_2$/SWNT xerogels with different $Ni(OH)_2$ loadings, a very high specific capacitance of above 7 F cm^{-2} has reached which surpasses the most previous reports.[13,50,52] The ultrahigh areal capacitances are obtained simply because of a high mass loading (5.59 mg cm^{-2}). However, with various deposition charges, only the NiC-xero-3.33 achieves good capacitance retention for an optimal mass loading (2.46 mg cm^{-2}).

In order to achieve a better understanding of the kinetic properties for the prepared samples, the EIS of the different composites are also measured as shown in Fig. 7. The estimated equivalent series resistance for $Ni(OH)_2$, NiC-xero and NiC-hydro are 1.21, 1.16 and 0.88 Ohm, respectively. The fitting

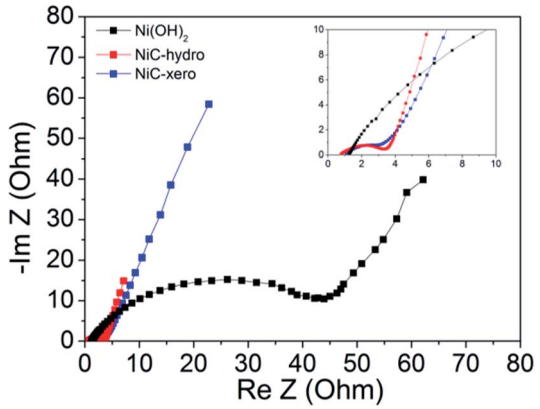

Fig. 7 Electrochemical impedance spectroscopy of NiC-xero, NiC-hydro and $Ni(OH)_2$.

results are presented in the Fig. S7a† according to a pre-built equivalent circuit (Fig. S7b†). For the $Ni(OH)_2$, which is much less porous than the NiC composite, we found it is difficult to fit the data to the as-established circuit and the equivalent series resistance is obtained based on the intercept with real part. Compared with the pure $Ni(OH)_2$ on the nickel foam, both NiC-xero and NiC-hydro composites demonstrate smaller charge transfer resistances (R_{ct}) of 0.87 and 1.60 Ohm estimated from the depressed semicircle. Such a small R_{ct} indicate a facilitated electron transport benefited from the SWNT scaffold. While for pure $Ni(OH)_2$, the electrons have to be delivered from the bottom of the nickel foam to the bulk $Ni(OH)_2$, and then to the layers contacted to the electrolyte, leading to a large R_{ct} around 40.77 Ohm. The 45° slope portion of the EIS curve connecting the semicircle (Warburg resistance) is related to the frequency dependent ion transport.

Fig. 8 presents the long term cycling performance at a constant charge/discharge rate of 10 mA cm^{-2}. The NiC-xero composite has the good capacitance retention of 85.2% after 1000^{th} cycle. For NiC-hydro composite, although it shows the highest specific capacitance at initial cycles, but capacitance dramatically deteriorates and preserves ~19.4% of its

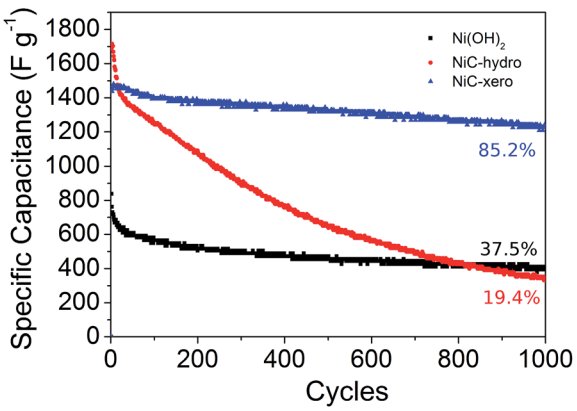

Fig. 8 Cycling performance of $Ni(OH)_2$, $Ni(OH)_2$/SWNT hydrogel and $Ni(OH)_2$/SWNT xerogel electrode.

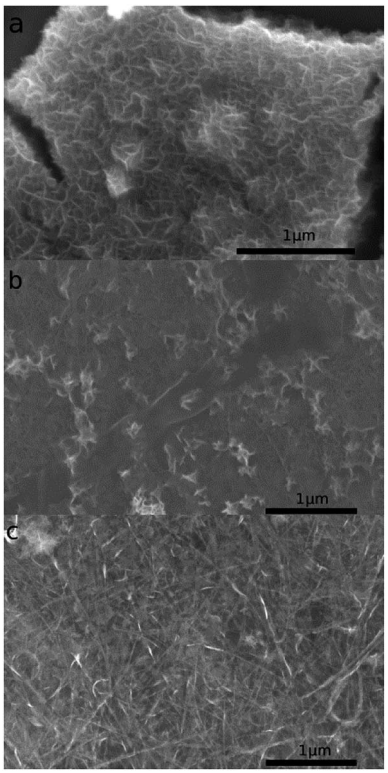

Fig. 9 SEM images of samples after cycling (a) $Ni(OH)_2$, (b) $Ni(OH)_2$/SWNT xerogel (NiC-xero) electrode and (c) $Ni(OH)_2$/SWNT hydrogel (NiC-hydro).

capacitance after 1000th cycle. Similarly, the capacitance of the pure $Ni(OH)_2$ decreases gradually to 37.5% of the initial capacitance after 1000th cycle. To explore the reasons of an improved cycling stability of NiC-xero composite, we have taken the FESEM images of the samples after cycling test as shown in Fig. 9. For the $Ni(OH)_2$, no major morphology change is observed (Fig. 9a). Its capacitance decreases possibly due to the $Ni(OH)_2$ detachment from the nickel foam.[52] For the SWNT-hydrogel composite, newly formed agglomerations of $Ni(OH)_2$ can be observed (Fig. 9c) along the nanotube bundles. After several cycles of charge/discharge, the phase transformation may generate strain which renders $Ni(OH)_2$ detach from the electrically conducting SWNT network, resulting in a poor electrochemical performance. In contrast, the SWNT-xerogel composite (Fig. 9b) has minor morphology change even after 1000th cycle for a better bonding between the $Ni(OH)_2$ because of a near flat SWNT bundle surface. In addition, the SWNT bundles in the porous structure of the xerogel composite contribute to serve as the buffer layers to accommodate the internal strain generated during the charge/discharge cycles and, thus, maintain the electrode stability.

4 Conclusions

In summary, we have successfully developed the 3D gel composite electrodes for the SC applications. Compared with the pure $Ni(OH)_2$ gels, the developed SWNT-hydrogel and xerogel composites demonstrate the better electrochemical performance because of their conductive 3D SWNTs networks. The roles of SWNTs during charge/discharge in xerogel composite are: (i) SWNTs help to improve the conductivity and thus, facilitate the electron transport during charge/discharge, (ii) SWNTs help to accommodate the volume change of $Ni(OH)_2$, serving as a buffer layer to improve the cycling stability.

Acknowledgements

The authors thank SERC 2011 PSF Funding, R-265-000-424-305 for the funding support and also thank Prof L. Lu, National University of Singapore for his kind help on academic discussion. Finally, we greatly appreciate Miss Fan Zeng (National University of Singapore) for her help on language modification.

References

1 J. R. Miller and P. Simon, *Science*, 2008, **321**, 651.
2 P. Simon and Y. Gogotsi, *Nat. Mater.*, 2008, **7**, 845.
3 L. L. Zhang and X. S. Zhao, *Chem. Soc. Rev.*, 2009, **38**, 2520.
4 A. Burke, *Electrochim. Acta*, 2007, **53**, 1083.
5 V. Augustyn, P. Simon and B. Dunn, *Energy Environ. Sci.*, 2014, **7**, 1597.
6 J. Yan, Q. Wang, T. Wei and Z. Fan, *Adv. Energy Mater.*, 2014, **4**, 1300816.
7 P. Simon, Y. Gogotsi and B. Dunn, *Science*, 2014, **343**, 1210.
8 C. Y. Foo, A. Sumboja, D. J. H. Tan, J. Wang and P. S. Lee, *Adv. Energy Mater.*, 2014, **4**, 1400236.
9 M. Sathiya and A. Prakash, *J. Am. Chem. Soc.*, 2011, **133**, 16291.
10 A. J. Bard and L. R. Faulkner, *Electrochemical Methods: Fundametals and Applications*, John Wiley & Sons, Inc, 2011.
11 J. Huang, P. Xu, D. Cao, X. Zhou, S. Yang, Y. Li and G. Wang, *J. Power Sources*, 2014, **246**, 371.
12 G. W. Yang, C. L. Xu and H. L. Li, *Chem. Commun.*, 2008, 6537.
13 Z. Pu, Q. Liu, A. H. Qusti, A. M. Asiri, A. O. Al-Youbi and X. Sun, *Electrochim. Acta*, 2013, **109**, 252.
14 X. Liu, S. Shi, Q. Xiong and L. Li, *ACS Appl. Mater. Interfaces*, 2013, **5**, 8795.
15 Z. Tang, C. Tang and H. Gong, *Adv. Funct. Mater.*, 2012, **22**, 1272.
16 C. Guan, J. Liu, C. Cheng, H. Li, X. Li, W. Zhou, H. Zhang and H. J. Fan, *Energy Environ. Sci.*, 2011, **4**, 4496.
17 X. Xia, J. Tu, Y. Mai, R. Chen, X. Wang, C. Gu and X. Zhao, *Chem.–Eur. J.*, 2011, **17**, 10898.
18 Y. Q. Zhao, D. D. Zhao, P. Y. Tang, Y. M. Wang, C. L. Xu and H. L. Li, *Mater. Lett.*, 2012, **76**, 127.
19 J. Ji, L. Zhang, H. Ji, Y. Li, X. Zhao and X. Bai, *ACS Nano*, 2013, **7**, 6237.
20 X. Cao, Y. Shi, W. Shi, G. Lu, X. Huang, Q. Yan, Q. Zhang and H. Zhang, *Small*, 2011, **7**, 3163.
21 M. Liu, S. He and W. Chen, *Nanoscale*, 2014, **6**, 11769.
22 H. Hu, S. Liu, M. Hanif, S. Chen and H. Hou, *J. Power Sources*, 2014, **268**, 451.

23 S. He and W. Chen, *J. Power Sources*, 2014, **262**, 391.
24 J. Chmiola, G. Yushin, Y. Gogotsi, C. Portet, P. Simon and P. L. Taberna, *Science*, 2006, **313**, 1760.
25 Z. Fan, D. Z. Y. Tng, S. T. Nguyen, J. Feng, C. Lin, P. Xiao, L. Lu and H. M. Duong, *Chem. Phys. Lett.*, 2013, **561**, 92.
26 L. Chen and Z. H. Huang, *Adv. Funct. Mater.*, 2014, **24**, 5104.
27 Y. Xu, Z. Lin, X. Huang, Y. Liu, Y. Huang and X. Duan, *ACS Nano*, 2013, **8**, 4042.
28 S. Ye, J. Feng and P. Wu, *ACS Appl. Mater. Interfaces*, 2013, **5**, 7122.
29 J. Chen, K. Sheng, P. Luo, C. Li and G. Shi, *Adv. Mater.*, 2012, **24**, 4569.
30 L. Wu, W. Li, P. Li, S. Liao, S. Qiu, M. Chen, Y. Guo, Q. Li, C. Zhu and L. Liu, *Small*, 2014, **10**, 1421.
31 H. Huang, Y. Tang and L. Xu, *ACS Appl. Mater. Interfaces*, 2014, **6**, 10248.
32 H. Huang, L. Xu, Y. Tang, S. Tang and Y. Du, *Nanoscale*, 2014, 2426.
33 H. Gao, F. Xiao, C. B. Ching and H. Duan, *ACS Appl. Mater. Interfaces*, 2012, **42012**, 2801.
34 S. Chen, J. Duan, Y. Tang and S. Zhang Qiao, *Chem.–Eur. J.*, 2013, **19**, 7118.
35 T. Zhai, F. Wang, M. Yu, S. Xie, C. Liang, C. Li, F. Xiao, R. Tang, Q. Wu, X. Lu and Y. Tong, *Nanoscale*, 2013, **5**, 6790.
36 J. Yuan, J. Zhu, H. Bi, Z. Zhang, S. Chen, S. Liang and X. Wang, *RSC Adv.*, 2013, **3**, 4400.
37 C. C. Wang, H. C. Chen and S. Y. Lu, *Chem.–Eur. J.*, 2014, **20**, 517.
38 Z. Zhang, F. Xiao, L. Qian, J. Xiao, S. Wang and Y. Liu, *Adv. Energy Mater.*, 2014, **4**, 140064.
39 M. B. Bryning, D. E. Milkie, M. F. Islam, L. A. Hough, J. M. Kikkawa and A. G. Yodh, *Adv. Mater.*, 2007, **19**, 661.
40 K. J. Zhang, A. Yadav, K. H. Kim, Y. Oh, M. F. Islam, C. Uher and K. P. Pipe, *Adv. Mater.*, 2013, 2926.
41 J. Zou, J. Liu, A. S. Karakoti, A. Kumar, D. Joung, Q. Li, S. I. Khondaker, S. Seal and L. Zhai, *ACS Nano*, 2010, **4**, 7293.
42 S. N. Schiffres, K. H. Kim, L. Hu, A. J. H. McGaughey, M. F. Islam and J. A. Malen, *Adv. Funct. Mater.*, 2012, **22**, 5251.
43 K. H. Kim, Y. Oh and M. F. Islam, *Nat. Nanotechnol.*, 2012, **7**, 562.
44 T. Kim, G. Jung, S. Yoo, K. Suh and R. Ruoff, *ACS Nano*, 2013, **7**, 6899.
45 P. Y. Chen, M. N. Hyder, D. Mackanic, N. M. D. Courchesne, J. Qi, M. T. Klug, A. M. Belcher and P. T. Hammond, *Adv. Mater.*, 2014, **26**, 5101.
46 L. A. Hough, M. F. Islam, B. Hammouda, A. G. Yodh and P. A. Heiney, *Nano Lett.*, 2006, **6**, 313.
47 D. Zhao, W. Zhou and H. Li, *Chem. Mater.*, 2007, **19**, 3882.
48 Q. Yao, Q. Wang, L. Wang and L. Chen, *Energy Environ. Sci.*, 2014, **7**, 3801.
49 J. Yan, Z. Fan, W. Sun, G. Ning, T. Wei, Q. Zhang, R. Zhang, L. Zhi and F. Wei, *Adv. Funct. Mater.*, 2012, **22**, 2632.
50 H. Cheng, A. D. Su, S. Li, S. T. Nguyen, L. Lu, C. Y. H. Lim and H. M. Duong, *Chem. Phys. Lett.*, 2014, **601**, 168.
51 W. Xing, S. Qiao, X. Wu, X. Gao, J. Zhou, S. Zhuo, S. B. Hartono and D. Hulicova-Jurcakova, *J. Power Sources*, 2011, **196**, 4123.
52 G. Hu, C. Li and H. Gong, *J. Power Sources*, 2010, **195**, 6977.